Electronic Supplementary Information

Reversing the Activity Landscape of MoS_x Electrocatalysts via Ni_xP Interfacial Coupling for Alkaline Hydrogen Evolution

Ioannis Vamvasakis,*[a] Aggelos Grammenos[b] and Gerasimos S. Armatas*[a]

[a] Department of Materials Science and Engineering, University of Crete, Vassilika Vouton, Heraklion 70013, Greece.
[b] Department of Chemistry, University of Crete, Vassilika Vouton, Heraklion 70013, Greece.
*Corresponding authors. E-mail address: j.vamvasakis@uoc.gr, garmatas@uoc.gr

Experimental Section

Chemicals and reagents

Sodium molybdate dihydrate ($Na_2MoO_4 \cdot 2H_2O$), nickel(II) chloride hexahydrate ($NiCl_2 \cdot 6H_2O$, ≥98%), iron(III) nitrate nonahydrate ($Fe(NO_3)_3 \cdot 9H_2O$), ≥98%), nickel(II) nitrate hexahydrate ($Ni(NO_3)_2 \cdot 6H_2O$, ≥98%), sodium hypophosphite monohydrate ($NaH_2PO_2 \cdot H_2O$, ≥99%), sodium sulfide nonahydrate ($Na_2S \cdot 9H_2O$, ≥98%), hydrochloric acid (HCl, ≥37%, ACS reagent grade), ammonium chloride (NH_4Cl), Nafion solution (5 wt.%), and deuterium oxide (D_2O, 99.8%) were purchased from Sigma-Aldrich. Ammonium hydroxide solution (≈25% NH_3 basis), ethanol (≥98%) and potassium hydroxide (KOH, ≥85%) were supplied by Honeywell. Pt/C (20 wt.%) was purchased from Johnson Matthey Chemicals Ltd. All chemical were used as received without further purification. Double distilled water was used in this work.

Synthesis of MoS_x-based catalysts

Preparation of precursor solutions

The tetrathiomolybdate precursor solution used for MoS_x electrodeposition was prepared by initially dissolving 2.25 mmol of Na_2MoO_4 in 40 mL of deionized (DI) water, forming solution A. In a separate beaker, 10 mmol of Na_2S were dissolved in 20 mL of DI water to obtain solution B. Subsequently, solutions A and B were combined under continuous stirring, and additional DI water was added to reach a final volume of 150 mL. The pH of the resulting mixture was adjusted to 8 using HCl. Upon pH adjustment, the solution color changed from colorless to dark red, indicating the formation of thiomolybdate species. The Ni-P precursor solution used for Ni_xP electrodeposition was prepared by dissolving 50 mmol of NH_4Cl in 200 mL of DI water. Subsequently, 5 mmol of $NiCl_2$ were added and allowed to fully dissolve. Finally, 50 mmol of NaH_2PO_2 were introduced into the solution. The pH was then adjusted to 9 using ammonium hydroxide, providing appropriate conditions for subsequent electrodeposition.

Synthesis of MoS_x

MoS_x films were deposited on carbon cloth (CC) substrates via potentiostatic electrodeposition using a three-electrode configuration. The CC substrate served as the working electrode (WE), carbon paper as the counter electrode (CE), and a saturated calomel electrode (SCE, sat. KCl, 0.244 V vs SHE) as the reference electrode (RE). Prior to deposition, the CC substrates (1 × 2 cm^2) were thoroughly cleaned by sequential ultrasonication in acetone, 2 M HCl, DI water, and ethanol for 15 min each solvent, followed by drying at 60 °C for 12 h. The pre-treated substrate (with an exposed geometric area of 1 cm^2) was then immersed in the tetrathiomolybdate precursor solution. Electrodeposition of MoS_x was carried out by chronoamperometry at a constant potential of −1.5 V vs SCE for 30 min at room temperature. The deposition time was selected based on preliminary electrocatalytic optimization studies (data not shown). After deposition, the WE was thoroughly rinsed with DI water and ethanol, and then dried at 60 °C overnight.

Synthesis of MoS_x-800

The MoS_x-800 sample was obtained by post-annealing an electrodeposited MoS_x electrode on CC, as described above. The as-prepared electrode was annealed at 800 °C for 2 h in a sulfur-rich Ar atmosphere using a tube furnace. To ensure a sulfur-rich environment during treatment, approximately 50 mg of sulfur

powder was placed in an alumina boat, with the sample electrode positioned above it. After annealing, the sample was thoroughly rinsed with DI water and ethanol, and then dried at 60 °C overnight.

Synthesis of MoS_x-hydro

The MoS_x-hydro electrode was synthesized via a hydrothermal method using the same tetrathiomolybdate precursor solution (pH=8) employed for electrodeposition. A pre-cleaned CC substrate was immersed in 15 mL of this solution inside a 25 mL Teflon-lined stainless-steel autoclave. The autoclave was heated at 200 °C for 14 h and then allowed to cool naturally to room temperature. The resulting electrode was removed, thoroughly rinsed with DI water and ethanol, and dried at 60 °C overnight.

For comparison, the powder precipitate formed during the hydrothermal process (denoted MoS_x-hydro-powder) was collected by centrifugation, washed several times with DI water and ethanol, and dried at 60 °C overnight.

Synthesis of Ni_xP-modified MoS_x catalysts

Ni_xP-modified MoS_x-based electrodes were prepared via electrodeposition using a conventional three-electrode configuration. The as-prepared MoS_x samples on CC substrates served as the WE, nickel foam as the CE, and an SCE as the RE. Each WE, with an exposed geometric area of 1 cm^2, was immersed in the nickel–hypophosphite precursor solution. Electrodeposition was performed galvanostatically at a constant current of −20 mA for 30 min at room temperature. The deposition time was selected based on preliminary optimization studies (data not shown). After deposition, the electrodes were thoroughly rinsed with DI water and ethanol, and then dried overnight at 60 °C. Using this procedure, a series of Ni_xP-modified MoS_x electrodes were fabricated, denoted as Ni_xP/MoS_x, Ni_xP/MoS_x-800, and Ni_xP/MoS_x-hydro, according to the respective MoS_x precursor.

For comparison, a bare Ni_xP reference electrode was prepared under identical conditions using a clean CC substrate as the WE. In addition, Ni/MoS_x and Ni-only control samples were synthesized following the same electrodeposition protocol using the nickel precursor solution without NaH_2PO_2.

Preparation of Pt/C catalyst

The Pt/C benchmark electrocatalyst was prepared by dispersing 5 mg of commercial 20 wt.% Pt/C powder in 1 mL of a water/ethanol mixture (1:3 v/v) containing 80 µL of 5 wt.% Nafion solution. The mixture was ultrasonicated for 30 min to obtain a homogeneous ink. Subsequently, 300 µL of the ink was drop-cast onto a pre-cleaned CC substrate with an exposed geometric area of 1 cm^2, followed by drying at 60 °C for 4 h.

Preparation of NiFe-LDH

The NiFe-layered double hydroxide (NiFe-LDH) electrode was synthesized via electrodeposition following the procedure of Quiroz et al.[1], with slight modifications. Briefly, the deposition was conducted in a standard three-electrode cell configuration, using a carbon plate as the CE, a SCE as the RE, and nickel foam (1 × 2 cm^2) as the WE. Prior to deposition, the nickel foam substrate was sequentially ultrasonicated in acetone, dilute HCl, and ethanol for 15 min in each solvent, and then dried at 80 °C for 30 min. The electrolyte solution (100 mL) contained $Ni(NO_3)_2$ and $Fe(NO_3)_3$ as metal precursors, with a Ni:Fe molar ratio of 15:1. Electrodeposition was carried out at a constant potential of −1.2 V vs SCE for 40 min at room temperature. After deposition, the electrode was thoroughly rinsed with DI water and ethanol, and then dried at 80 °C for 60 min. The effective deposition area was maintained at 1 × 1 cm^2 throughout the process.

Materials characterizations

Field-emission scanning electron microscopy (SEM) and energy-dispersive X-ray spectroscopy (EDS) were carried out using a JEOL JSM-IT700HR microscope operated at 20 kV. EDS data acquisition was conducted from multiple areas of each sample using an accelerating voltage of 20 kV and a 60-s accumulation time. X-ray diffraction (XRD) patterns were collected on a Rigaku SmartLab X-ray diffractometer using Cu Kα radiation (λ=1.5406 Å), operated at 40 kV and 50 mA. Raman measurements at room temperature were performed with a Thermo Scientific DXR3xi Raman imaging microscope equipped with a 532 nm laser. The laser power was maintained at 3 mW for maximum clarity and measurements were carried out with an Olympus 50× objective with 0.8 numerical aperture. X-ray photoelectron spectroscopy (XPS) was performed on a SPECs spectrometer equipped with a Phoibos 100 1D-DLD electron analyser using monochromatic Al Kα radiation (hv=1486.6 eV). Analyses were performed on freshly prepared samples with particular care taken to minimize air exposure prior to measurement. All

binding energies were calibrated against the adventitious C 1s peak at 284.8 eV. Peak deconvolution was conducted with SpecsLab Prodigy software using Gaussian-Lorentzian line profiles after Shirley background substation.

Electrochemical measurements

The electrocatalytic hydrogen evolution reaction (HER) performance of all prepared catalysts was evaluated in an alkaline electrolyte (1.0 M KOH, pH=14) at room temperature using a simple one-compartment three-electrode system connected to a VersaSTAT 4 electrochemical workstation (Princeton Applied Research). The three-electrode setup comprised the as-prepared catalysts deposited on CC (1 cm^2 geometric area) as the WE, a carbon rod as the CE, and a Hg/HgO electrode (in 1.0 M KOH) as the RE. Polarization curves were obtained via linear sweep voltammetry (LSV) at a scan rate of 5 mV s^{-1}. All measurements were repeated at least three times to ensure reproducibility. The measured potentials were corrected for *iR* drop using the uncompensated solution resistance (R_s) determined via electrochemical impedance spectroscopy (EIS) and were converted to the reversible hydrogen electrode (RHE) scale using the following equation:

$$E_{RHE} = E_{Hg/HgO} + 0.098 + 0.059 \times pH \text{ (at 25 °C)} \quad (1)$$

where, $E_{Hg/HgO}$ is the measured potential versus the Hg/HgO reference electrode, and E_{RHE} is the potential converted to the RHE scale.

Tafel slopes were determined by fitting the linear portion of the Tafel plots using:

$$\eta = b \cdot \log|J| + \alpha \quad (2)$$

where η is the overpotential (V) calculated by $\eta = 0 - E_{RHE}$, J is the current density (mA cm^{-2}), b is the Tafel slope (mV dec^{-1}), and α is a constant.

Electrochemical stability was evaluated by chronopotentiometry in 1.0 M KOH at a constant current density of −10 mA cm^{-2}.

Electrochemically active surface area (ECSA) was estimated from the double-layer capacitance (C_{dl}), which was determined by cyclic voltammetry (CV) measurements performed in 1.0 M KOH at scan rates ranging from 20 to 180 mV s^{-1}. These measurements were conducted within a non-Faradaic potential window (–0.15 V to –0.25 V vs Hg/HgO). The capacitive current density (j) is linearly proportional to the scan rate (v), and C_{dl} was obtained from the slope of the plot of current density difference ($\Delta j = (j_a - j_c)/2$) versus v, according to:

$$C_{dl} = \frac{|j_a - j_c|}{2v} \quad (3)$$

where j_a and j_c are the anodic and cathodic current densities at the midpoint of the potential window, respectively.

The ECSA is then calculated by:

$$ECSA = \frac{A \cdot C_{dl}}{C_s} \quad (4)$$

where A is the geometric surface area (cm^2) and C_s is the specific capacitance of a flat surface of an electrode material, with a typical reported value of 0.040 mF cm^{-2} in alkaline solutions.[2]

EIS measurements were carried out in 1.0 M KOH using a standard three-electrode configuration over a frequency range of 100 kHz to 0.1 Hz, with a 10 mV AC perturbation. For conventional EIS measurements, a DC bias of −1.2 V vs Hg/HgO was applied, while a range of applied potentials was used in operando EIS experiments.

Kinetic isotope effect (KIE = J_{H2O}/J_{D2O}) measurements were performed using LSV in both 1.0 M KOH/H_2O and 1.0 M KOH/D_2O electrolytes under identical conditions. A three-electrode cell was employed, in which

the catalyst-loaded CC served as the WE, and a Hg/HgO (1.0 M KOH) electrode and a Pt wire were used as the RE and CE, respectively. LSV scans were recorded at a scan rate of 5 mV s^{-1}.

Supporting figures and tables

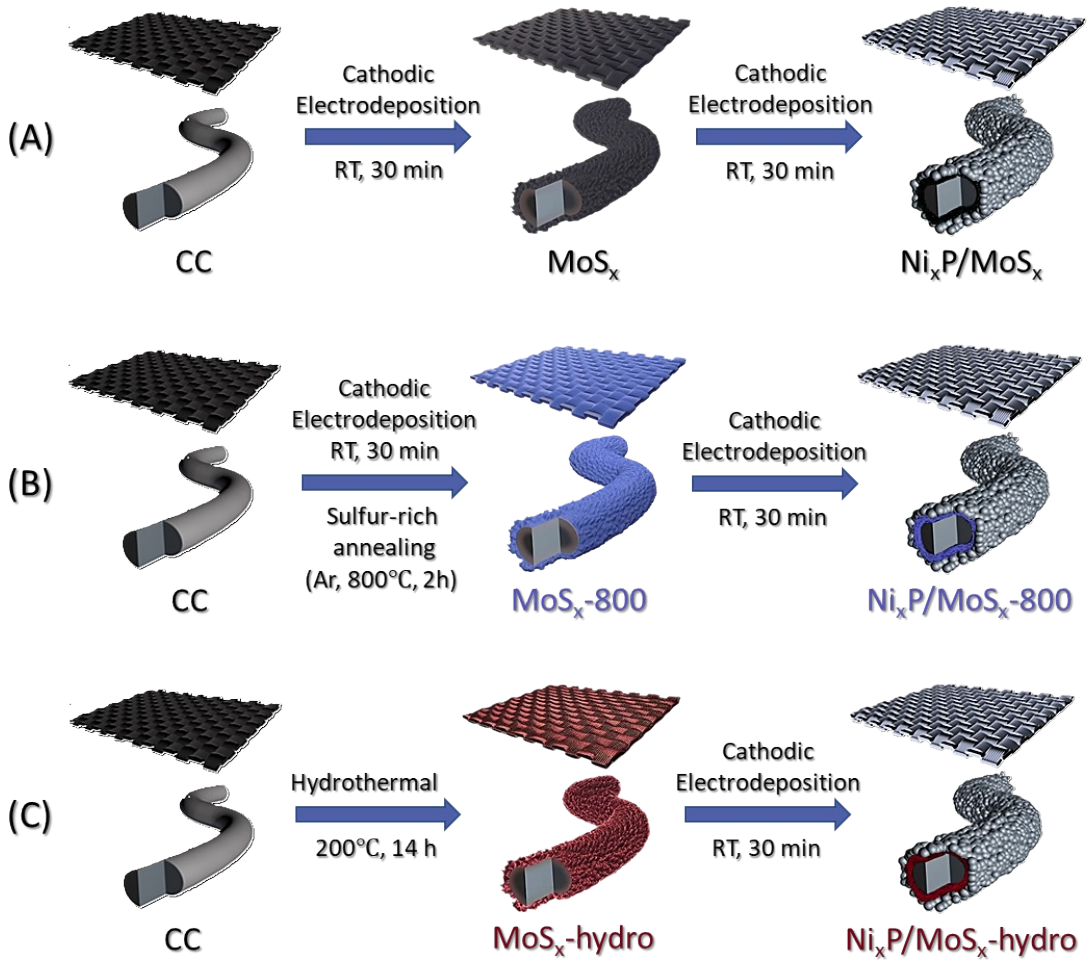

Fig. S1. Schematic illustration of the synthesis procedures: (A) cathodic electrodeposition of MoS_x and subsequent deposition of Ni_xP to form Ni_xP/MoS_x on carbon cloth (CC), (B) preparation of MoS_x-800 via cathodic electrodeposition followed by sulfur-rich annealing under Ar-atmosphere at 800 °C, and subsequent Ni_xP deposition to yield Ni_xP/MoS_x-800, and (C) hydrothermal synthesis of MoSx-hydro on CC, followed by Ni_xP electrodeposition to obtain Ni_xP/MoS_x-hydro.

Fig. S1 illustrates the synthesis procedure of Ni_xP-modified MoS_x catalysts. Initially, three MoS_x-based electrodes were prepared on carbon cloth (CC), followed by surface modification through deposition of a Ni_xP overlayer. The first electrode (MoS_x) was prepared via a single-step cathodic electrodeposition at room temperature, based on the electrochemical reduction of tetrathiomolybdate ions (MoS_4^{2-}) on the CC substrate (Fig. S1a):

$$MoS_4^{2-} + 2e^- + 2H_2O \rightarrow MoS_2 + 2SH^- + 2OH^- \quad (5)$$

The tetrathiomolybdate precursors were generated by reacting molybdate (MoO_4^{2-}) with excess sulfide (S^{2-}) under mildly acidic conditions (Eq. 6). The precursor solution was prepared by dissolving Na_2MoO_4 and excess Na_2S in water, followed by pH adjustment to 8 using HCl. The observed color transition from colorless to dark red indicated the formation of thiomolybdate species:

$$MoO_4^{2-} + 4S^{2-} + 4H_2O \rightarrow MoS_4^{2-} + 8OH^- \quad (6)$$

As previously reported, MoS_x layers obtained via MoS_4^{2-} electrodeposition are typically X-ray amorphous with composition close to MoS_2.[34]
The second electrode (MoS_x-800) was obtained by annealing the as-deposited MoS_x at 800 °C for 2 h under a sulfur-rich Ar atmosphere (Fig. S1b).
The third electrode (MoS_x-hydro) was synthesized via a hydrothermal method (Fig. S1C), involving the growth of MoS_2 nanosheets directly on CC fibers at 200 °C for 14 h using the same MoS_4^{2-} precursor solution (pH=8). The simplified reaction pathway is:

$$MoS_4^{2-} + H_2O \rightarrow MoS_2 + HS^- + S + OH^- \quad (7)$$

Finally, all MoS_x electrodes were modified by galvanostatic electrodeposition of Ni_xP at room temperature to yield Ni_xP/MoS_x, Ni_xP/MoS_x-800 and Ni_xP/MoS_x-hydro heterostructures. This process involves the cathodic co-deposition of Ni and P species[5], as described by:

$$H_2PO_2^- + Ni^{2+} + 2NH_4^+ + 3e^- \rightarrow \text{Ni-P (layer)} + 2NH_3 + 2H_2 \quad (8)$$

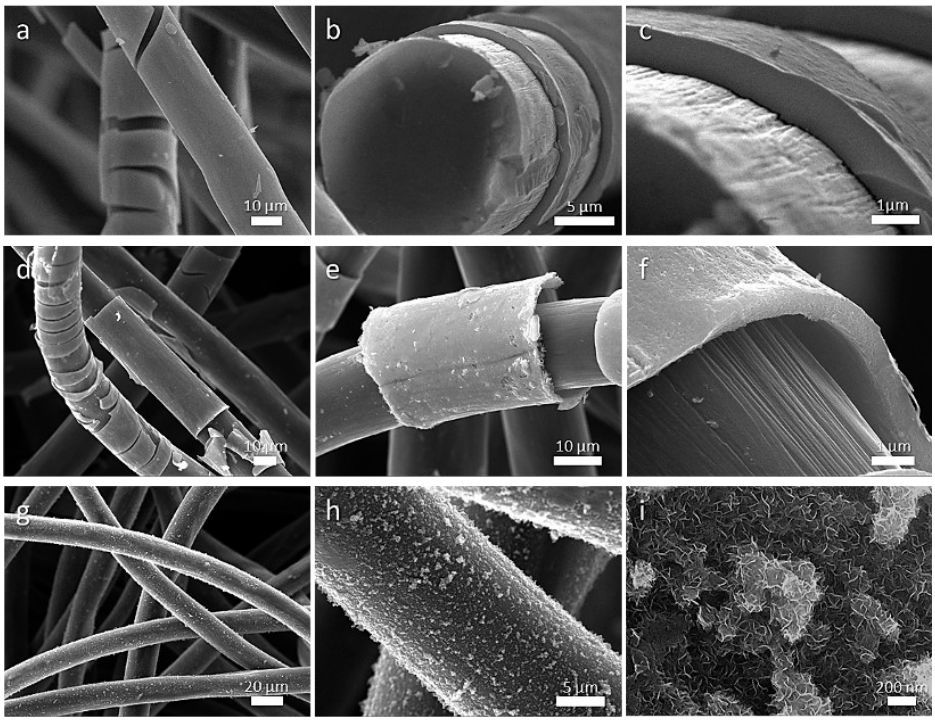

Fig. S2. Representative SEM images of as-synthesized MoS_x samples on carbon cloth (CC): (a–c) electrodeposited MoS_x, (d–f) thermally annealed MoS_x-800, and (g–i) the hydrothermally synthesized MoS_x-hydro.

SEM images of the electrodeposited MoS_x (Fig. S2a–c) reveal a uniform, featureless film conformally coating the carbon cloth (CC) fibers, with a thickness of ≈0.8–1 µm (Fig. S2c). This homogeneous coverage indicates efficient nucleation and growth during electrodeposition process. Localized shearing and tearing are evident, which can be attributed to shrinkage-induced mechanical stress during drying. Importantly, high-magnification imaging (Fig. S2c) confirms intimate interfacial contact between the MoS_x layer and the CC substrate, which is expected to minimize contact resistance and promote charge transfer during electrochemical operation. Following annealing at 800 °C, the MoS_x-800 sample (Fig. S2d–f) largely preserves a smooth surface morphology but exhibits increased fragmentation, as evidenced by more pronounced cracking and shearing (Fig. S2d,e). The film thickness decreases by ≈25% (Fig. S2f), consistent with thermally induced densification. In contrast, the hydrothermally synthesized MoS_x-hydro sample displays a distinctly different morphology (Fig. S2g–i). Although maintaining full coverage of the CC

fibers, the surface exhibits a rough, hierarchical textured structure (Fig. S2g,h). High-magnification images (Fig. S2i) reveal vertically aligned nanosheets extending from the fiber surface, resulting in a high density of exposed edge sites.

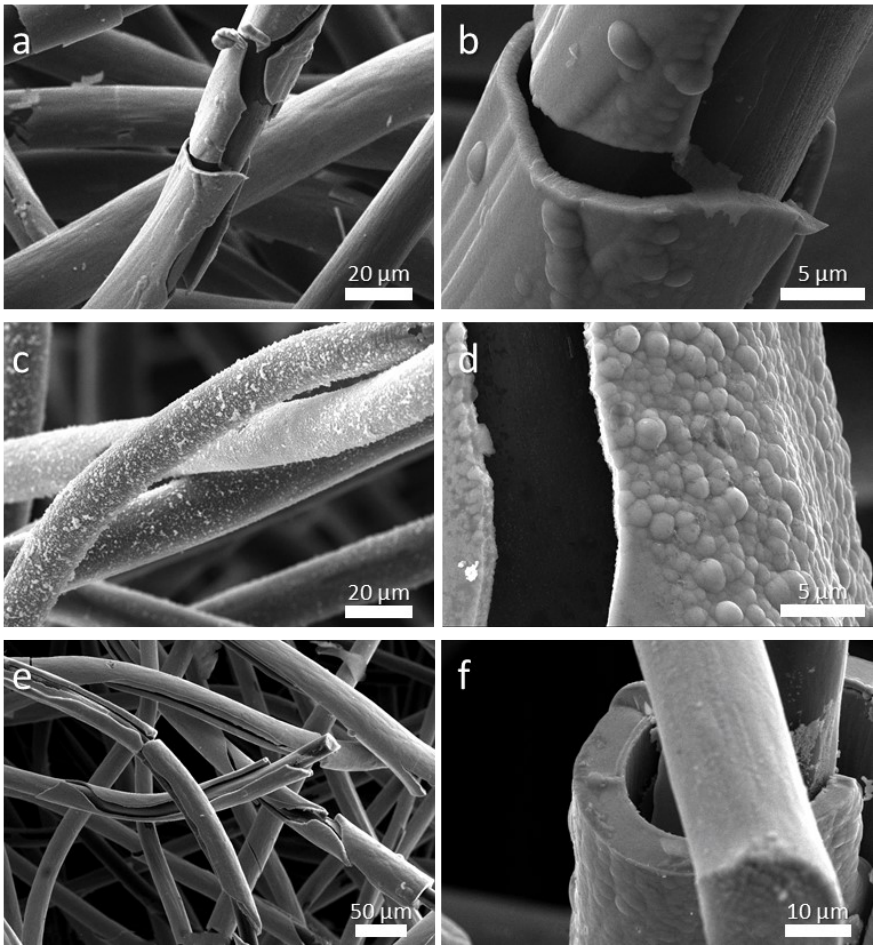

Fig. S3. Representative SEM images of (a, b) Ni_xP/MoS_x-800, (c, d) Ni_xP/MoS_x-hydro, and (e, f) Ni_xP deposited directly on carbon cloth (CC).

Following *in situ* electrodeposition of Ni_xP onto the different MoS_x electrodes, distinct morphological variations are observed, highlighting the critical role of the underlying MoS_x structure in governing Ni_xP nucleation and growth behavior. Ni_xP/MoS_x exhibits a roughened surface composed of densely distributed Ni_xP nanoparticles (Fig. 1a,b), whereas deposition on MoS_x-800 (Fig. S3a,b) yields a comparatively smoother and thicker Ni_xP overlayer. High-magnification imaging (Fig. S3b) suggests partial coalescence of the nanoparticles into a more continuous film, resembling the morphology of Ni_xP electrodeposited directly onto bare carbon cloth (Fig. S3e,f). In contrast, the Ni_xP /MoS_x-hydro sample (Fig. S3c,d) preserves the nanosheet framework of the hydrothermally growth MoS_x. In this case, Ni_xP nanoparticles conformally decorate the nanosheet surface. High-magnification image (Fig. S3d) reveals a characteristic knobby outer-layer morphology that closely follows the contours of the underlying nanosheets.

Table S1. Elemental composition of MoS_x, MoS_x-800 and MoS_x-hydro samples, together with their corresponding Ni_xP-modified heterostructures, determined by EDS analysis. Data for the Ni_xP-only electrode and post-stability Ni_xP/MoS_x sample are also given.

Sample	Mo (at%)	S (at%)	Ni (at%)	P (at%)	Mo:S ratio	Ni:P ratio
MoS_x	40.82	59.18	-	-	1:1.4	-
MoS_x-800	35.79	64.21	-	-	1:1.8	-
MoS_x-hydro	33.43	66.57	-	-	1:2.0	-
Ni_xP	-	-	89.92	10.08	-	9:1
Ni_xP/MoS_x	2.70	3.73	87.33	6.25	1:1.4	14:1
Ni_xP/MoS_x-800	1.92	3.54	86.70	7.84	1:1.8	11:1
Ni_xP/MoS_x-hydro	1.76	3.58	88.47	6.19	1:2.0	14:1
Ni_xP/MoS_x after long-term HER	2.28	5.36	86.36	6.00	1:2.0	14:1

EDS analysis confirms the presence of Mo and S in all MoS_x samples, with Mo:S ratios approaching the 1:2 stoichiometry of MoS_2 (Table S1). The electrodeposited MoS_x sample is substoichiometric (Mo:S ≈ 1:1.4 ± 0.07), indicative of sulfur-deficient structure, which are been widely reported to enhance HER activity.[6–8] Upon annealing at 800 °C in a sulfur-rich atmosphere, the MoS_x-800 sample exhibits an increased sulfur content (Mo:S ≈ 1:1.8 ± 0.01), while the hydrothermally synthesized MoS_x-hydro approaches near-stoichiometric composition (Mo:S ≈ 1:2 ± 0.13), consistent with the formation of MoS_2-like phases. Following Ni_xP deposition, EDS spectra show a marked attenuation of Mo and S signals, accompanied by dominant Ni and P contributions. This behavior arises from X-ray attenuation by the surface Ni_xP overlayer, which partially absorbs emissions from the underlying MoS_x layer, a well-recognized limitation of SEM-EDS analysis in multilayered structures.[6–8] Importantly, the Mo:S ratios remain essentially unchanged (1:1.4, 1:1.8, and ≈1:2 for Ni_xP/MoS_x, Ni_xP/MoS_x-800, and Ni_xP/MoS_x-hydro, respectively), indicating preservation of the underlying MoS_x composition during Ni_xP electrodeposition. The Ni_xP-containing samples exhibit Ni-rich compositions, with Ni:P ratios of 9:1 for Ni_xP, 11:1 for Ni_xP/MoS_x-800, and 14:1 for both Ni_xP/MoS_x and Ni_xP/MoS_x-hydro. These values are consistent with the formation of Ni–P alloy-like coatings rather than stoichiometric nickel phosphides, in line with typical electrodeposited Ni–P films, where P is incorporated as a minor component (typically 6–24 at%).[9,10] Notably, the higher Ni:P ratios observed for the heterostructures relative to Ni_xP deposited on bare carbon cloth suggest that the MoS_x surface affects nucleation dynamics, promoting preferential Ni deposition during the early stages of electrodeposition. This effect likely arises from initial Ni nucleation at MoS_x active sites, followed by Ni–P growth. This behavior likely involves initial Ni nucleation at active sites on MoS_x, followed by subsequent Ni–P co-deposition, ultimately yielding Ni-enriched overlayers. The similar Ni:P ratios (≈14:1) for Ni_xP/MoS_x and Ni_xP/MoS_x-hydro are consistent with their comparable nanoparticulate morphologies, whereas the lower ratio observed for Ni_xP/MoS_x-800 (≈11:1) correlates with its more compact coating. These results confirm the formation of well-defined Ni_xP/MoS_x heterostructures, in which the MoS_x layer retains its composition while the Ni_xP overlayer forms a Ni-rich, alloy-like coating governed by substrate-dependent nucleation mechanism.

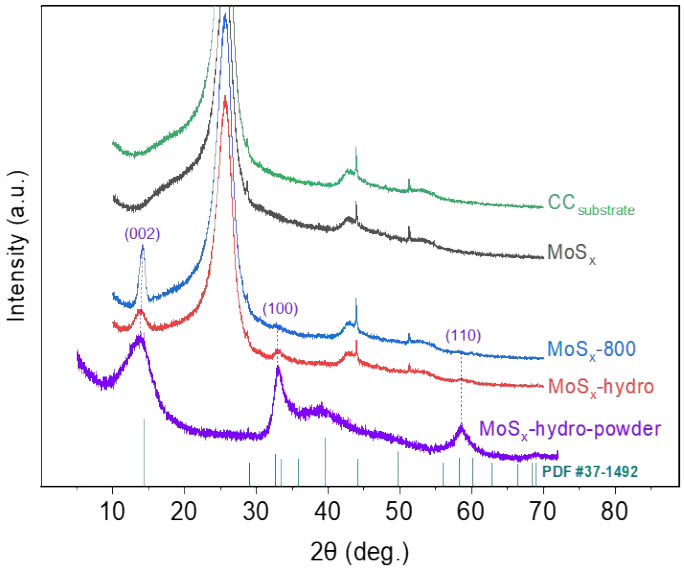

Fig. S4. X-ray diffraction (XRD) patterns of MoS_x, MoS_x-hydro and MoS_x-800. For comparison, XRD patterns of bare carbon cloth (CC), the hydrothermally synthesized MoS_x powder (MoS_x-hydro-powder), and the reference 2H-MoS_2 phase (PDF #37-1392) are also included.

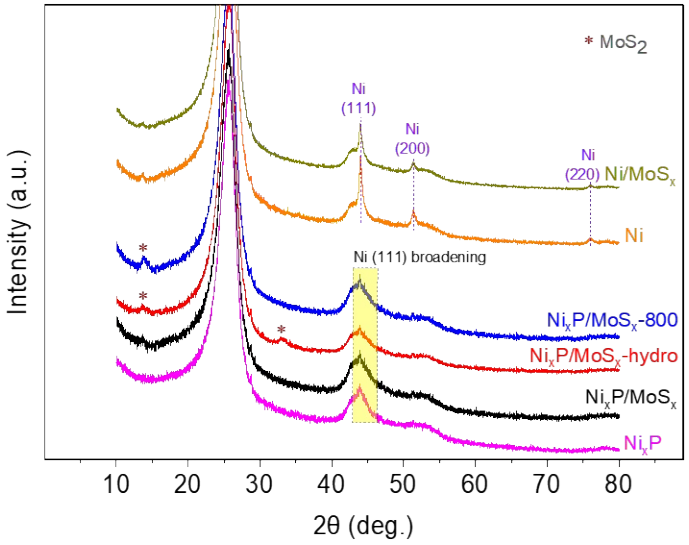

Fig. S5. X-ray diffraction (XRD) patterns of Ni_xP-modified MoS_x, MoS_x-hydro and MoS_x-800 hetero-structures. For comparison, XRD patterns of electrodeposited Ni on carbon cloth (CC) and Ni/MoS_x control samples are also included.

All Ni_xP-containing samples display a broad diffraction feature at 2θ ≈ 44°, which is attributed to the (111) reflection of Ni. The pronounced peak broadening indicates that the deposited Ni_xP phase is predominantly amorphous or nanocrystalline in nature, with only a minor contribution from crystalline Ni domains. In contrast, Ni/MoS_x and Ni-only control samples exhibit well-defined, sharp reflections at 2θ ≈ 44°, 51° and 76°, corresponding to the (111), (200) and (220) planes of face-centered cubic (fcc) Ni, respectively.

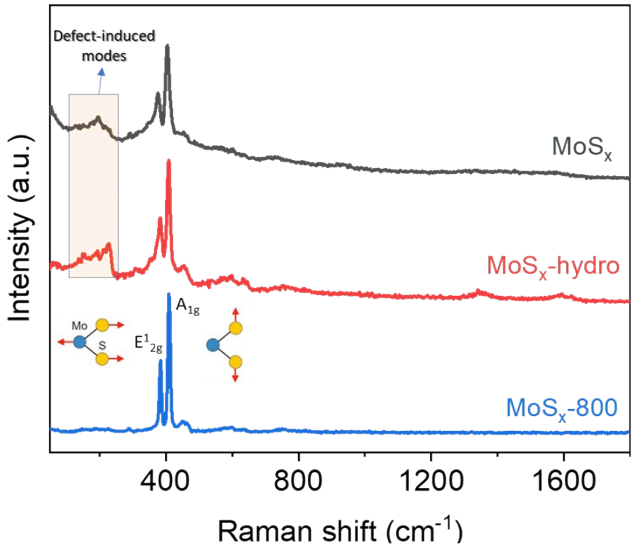

Fig. S6. Raman spectra of as-synthesized MoS_x, MoS_x-hydro and MoS_x-800.

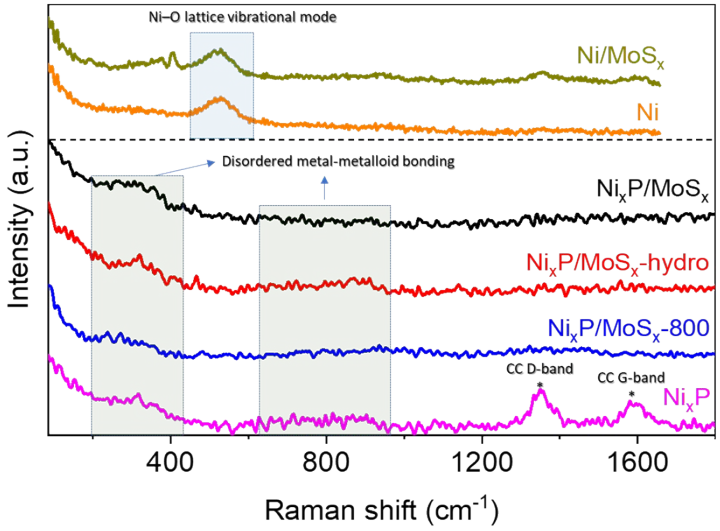

Fig. S7. Raman spectra of Ni_xP-modified MoS_x, MoS_x-hydro and MoS_x-800 samples. For comparison, spectra of Ni_xP, Ni-only, and Ni/MoS_x control samples are also included. The Ni_xP spectrum is dominated by the characteristic D (≈1350 cm^{-1}, disordered sp^3-hybridized carbon) and G (≈1580 cm^{-1}, graphitic sp^2-hybridized carbon) bands of carbon, originating from the underlaying carbon cloth substrate.

Table S2. XPS fitting parameters results and peak assignments for MoS_x, Ni_xP and Ni_xP/MoS_x.

Sample	Peak		Binding Energy (eV)	Assignment to chemical species
MoS_x	Mo 3d	$3d_{5/2}$	229.8	Mo^{4+}
		$3d_{3/2}$	232.6	
		$3d_{5/2}$	230.8	Mo^{5+}
		$3d_{3/2}$	234.1	
		$3d_{5/2}$	232.7	Mo^{6+}
		$3d_{3/2}$	235.5	
	S 2s	peak 1	226.4	S 2s

	S 2p	$2p_{3/2}$	162.4	Unsaturated S^{2-}
		$2p_{1/2}$	163.6	
		$2p_{3/2}$	163.8	Terminal S_2^{2-}
		$2p_{1/2}$	165.1	
		peak 5	169.0	SO_x species
Ni_xP	Ni 2p	$2p_{3/2}$	852.6	Ni^0 (Ni-P)
		$2p_{1/2}$	869.8	
		$2p_{3/2}$	856	NiO_x species
		$2p_{1/2}$	873.7	
		sat. 1	861.9	Satellites
		sat. 2	880.3	
	P 2p	$2p_{3/2}$	129.5	P-Metal bond (Ni-P)
		$2p_{1/2}$	130.4	
		peak 3	133.0	PO_x species
Ni_xP/MoS_x	Mo 3d	$3d_{5/2}$	228.6	Mo^{4+}
		$3d_{3/2}$	231.8	
		$3d_{5/2}$	232.5	Mo^{6+}
		$3d_{3/2}$	235.6	
	S 2s	peak 1	226.1	S 2s
	S 2p	$2p_{3/2}$	161.9	Unsaturated S^{2-}
		$2p_{1/2}$	163.0	
		$2p_{3/2}$	163.7	Terminal S_2^{2-}
		$2p_{1/2}$	165.0	
		peak 5	168.1	SO_x species
	Ni 2p	$2p_{3/2}$	852.9	Ni^0 (Ni-P)
		$2p_{1/2}$	870.2	
		$2p_{3/2}$	856.0	NiO_x species
		$2p_{1/2}$	873.8	
		sat. 1	861.7	Satellites
		sat. 2	880.2	
	P 2p	$2p_{3/2}$	129.8	P-Metal bond (Ni-P)
		$2p_{1/2}$	130.7	
		peak 3	133	PO_x species
Ni_xP/MoS_x after long-term HER	Mo 3d	$3d_{5/2}$	228.7	Mo^{4+}
		$3d_{3/2}$	231.9	
	S 2p	peak 1	168.3	SO_x species
	Ni 2p	$2p_{3/2}$	855.5	Ni^{2+} species (hydroxylated Ni)
		$2p_{1/2}$	872.9	
		sat. 1	861.3	Satellites
		sat. 2	879.5	
	P 2p	$2p_{3/2}$	129.6	P-Metal bond (Ni-P)
		$2p_{1/2}$	130.8	
		peak 3	133.2	PO_x species

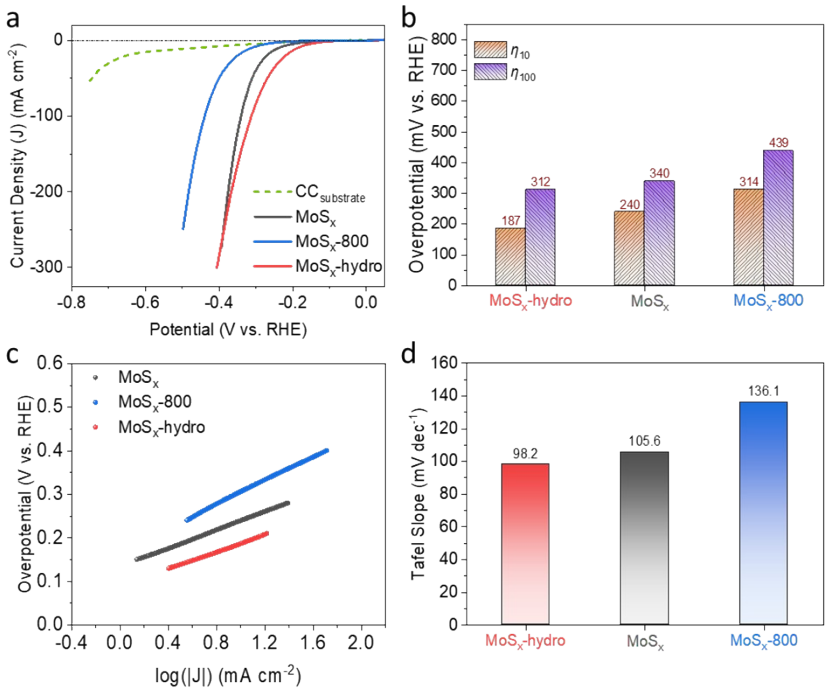

Fig. S8. (a) *iR*-corrected LSV curves measured in 1.0 M KOH and (b) corresponding overpotentials at –10 and –100 mA cm^{-2} (η_{10} and η_{100}) for the different MoS_x catalysts and bare carbon cloth (CC). (c) Tafel plots and (d) corresponding Tafel slopes of the different MoS_x catalysts.

Table S3. Comparison of HER performance of representative Ni_xP-modified MoS_2-based electrocatalysts.

Sample	**Overpotential η_{10} (mV)**	**Electrolyte**	**Reference**
Hierarchical Ni_2P/MoS_2	≈200	0.5 M H_2SO_4	11
Ni-P/MoS_x hybrid	140	1.0 M KOH	12
Ni_2P@MoS_2/CC	99	1.0 M KOH	13
NiP_x/MoS_2/CC hybrid	88	1.0 M KOH + 0.33M Urea	14
3D/2D Ni_2P@MoS_2	181	1.0 M KOH	15
Ni_2P-MoS_2 heteronanosheet arrays	78	1.0 M KOH	16
Ni_2P-black phosphorus (BP)/MoS_2	99	1.0 M KOH	17
Ni_3S_2@Ni_2P/MoS_2	160	1.0 M KOH	18
Amorphous Ni_xP/MoS_x	**96**	**1.0 M KOH**	**This work**

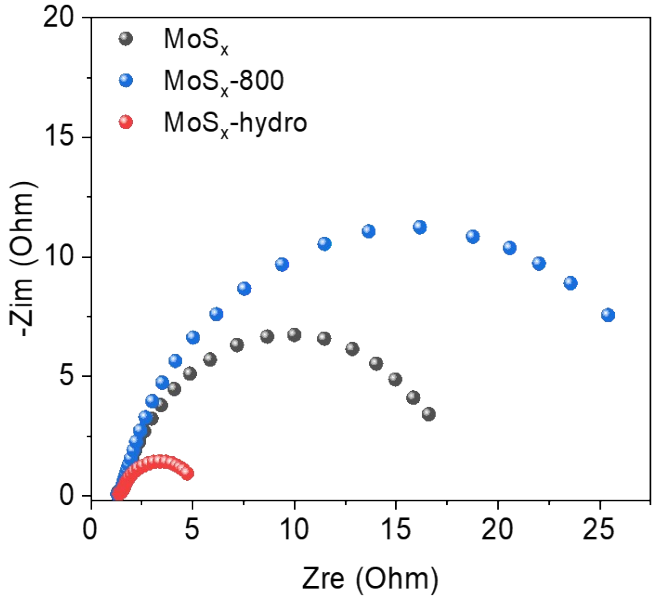

Fig. S9. EIS Nyquist plots of pristine MoS_x, MoS_x-hydro and MoS_x-800.

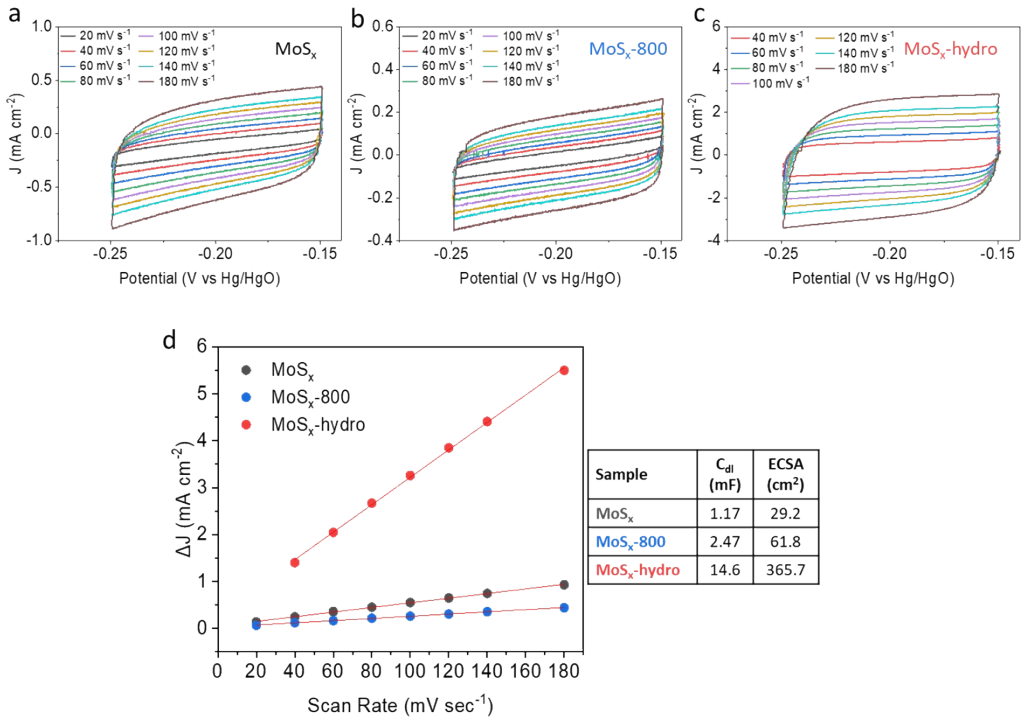

Sample	C_{dl} (mF)	ECSA (cm^2)
MoS_x	1.17	29.2
MoS_x-800	2.47	61.8
MoS_x-hydro	14.6	365.7

Fig. S10. (a-c) Cyclic voltammetry (CV) curves, (d) corresponding plot of capacitive current density (ΔJ) versus scan rate, used to determine the double-layer capacitance (C_{dl}) and estimate the electrochemically active surface area (ECSA) of MoS_x, MoS_x-hydro and MoS_x-800. Inset: calculated C_{dl} and ECSA values.

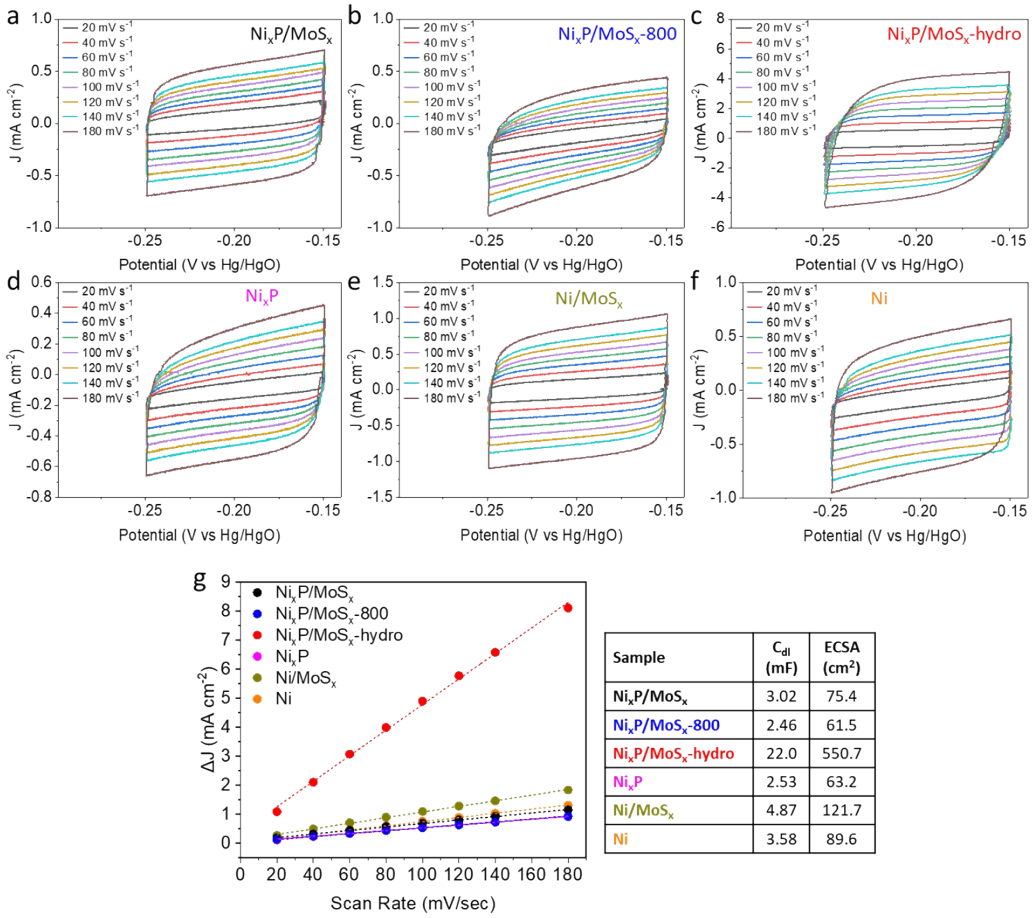

Sample	C_{dl} (mF)	ECSA (cm^2)
Ni_xP/MoS_x	3.02	75.4
Ni_xP/MoS_x-800	2.46	61.5
Ni_xP/MoS_x-hydro	22.0	550.7
Ni_xP	2.53	63.2
Ni/MoS_x	4.87	121.7
Ni	3.58	89.6

Fig. S11. (a-f) Cyclic voltammetry (CV) curves and (g) corresponding plot of capacitive current density (ΔJ) versus scan rate, used to determine the double-layer capacitance (C_{dl}) and estimate the electrochemically active surface area (ECSA) of the different Ni_xP-modified MoS_x catalysts and Ni_xP, Ni, and Ni/MoS_x control samples. Inset: calculated C_{dl} and ECSA values.

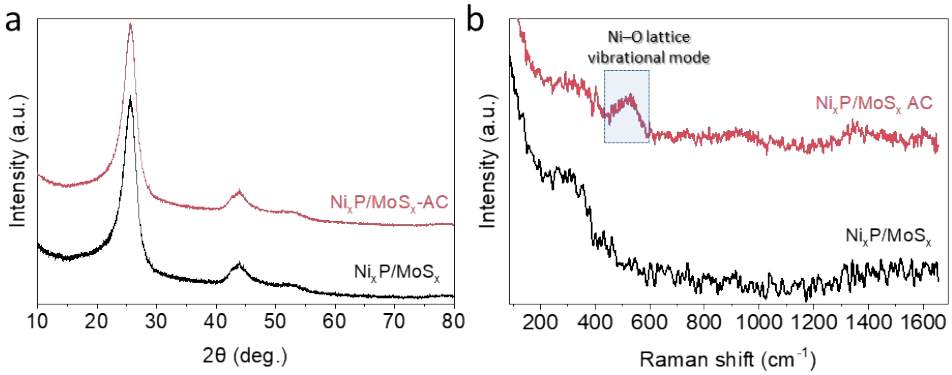

Fig. S12. (a) XRD patterns and (b) Raman spectra of Ni_xP/MoS_x before and after (Ni_xP/MoS_x AC) long-term HER testing.

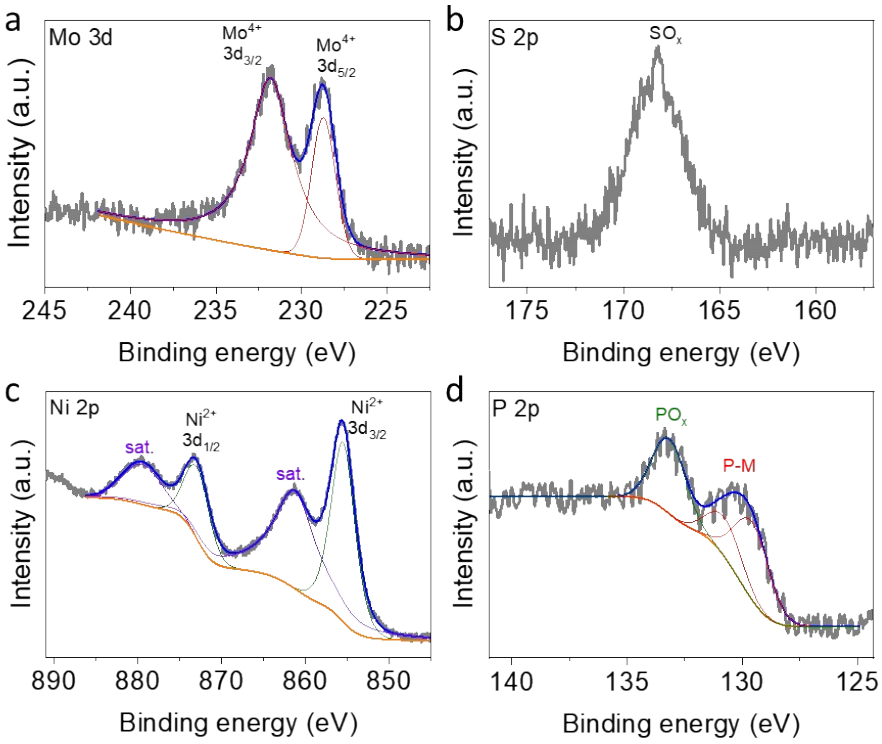

Fig. S13. XPS spectra of Ni_xP/MoS_x after long-term HER testing: (a) Mo 3d, (b) S 2p, (c) Ni 2p and (d) P 2p core-level spectra.

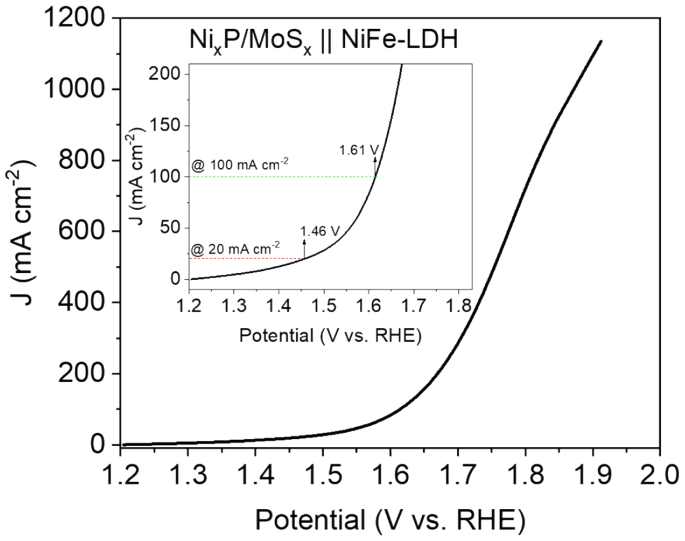

Fig. S14. Overall water-splitting polarization curve in 1.0 M KOH of the Ni_xP/MoS_x || NiFe-LDH cell, using Ni_xP/MoS_x on carbon cloth as the cathode and NiFe-LDH on nickel foam as the anode. Inset: enlarged view showing cell voltages at 20 and 100 mA cm^{-2}.

Table S4. Operando EIS fitting parameters for MoS_x and Ni_xP/MoS_x, obtained using the Armstrong–Henderson equivalent circuit. (R_s denotes the solution resistance, Q_{dl} describe the non-ideal double-layer capacitance, R_{ct} the interfacial charge-transfer resistance, while R_{ad} and C_{ad} describe the respective adsorption pseudo-resistance and pseudo-capacitance of H* intermediates).

MoS_x							
Potential (V vs RHE)	**R_s (Ω)**	**Q_{dl} [$mF \cdot s^{(a-1)}$]**	**a**	**R_{ct} (Ω)**	**C_{ad} (mF)**	**R_{ad} (Ω)**	**x^2**
0	1.71	38.1	0.89	3.99	10.02	274.7	4.3×10^{-3}
-0.05	1.70	40.5	0.90	4.07	10.80	212.7	4.7×10^{-3}
-0.10	1.70	39.7	0.91	3.89	11.97	93.59	5.1×10^{-3}
-0.15	1.70	37.1	0.93	2.90	13.92	34.38	5.6×10^{-3}
-0.20	1.70	41.7	0.91	1.69	16.84	14.23	4.3×10^{-3}
-0.25	1.71	42.6	0.89	0.99	22.02	4.01	2.5×10^{-3}
-0.30	1.70	43.6	0.85	0.67	25.03	1.34	9.9×10^{-4}
-0.35	1.71	27.7	0.83	0.69	24.84	0.77	5.5×10^{-4}
-0.40	1.70	39.1	0.85	0.46	32.45	0.67	1.2×10^{-3}
Ni_xP/MoS_x							
Potential (V vs RHE)	**R_s (Ω)**	**Q_{dl} [$mF \cdot s^{(a-1)}$]**	**a**	**R_{ct} (Ω)**	**C_{ad} (mF)**	**R_{ad} (Ω)**	**x^2**
0	1.31	150.6	0.90	0.43	60.76	51.35	6.9×10^{-4}
-0.05	1.31	154.6	0.88	0.35	61.28	26.58	4.7×10^{-4}
-0.10	1.30	171.4	0.83	0.27	62.40	5.97	2.0×10^{-4}
-0.15	1.31	180.9	0.82	0.30	62.61	1.79	3.7×10^{-4}
-0.20	1.31	180.4	0.82	0.31	77.70	0.77	3.2×10^{-4}
-0.25	1.31	160.1	0.82	0.22	95.77	0.47	3.9×10^{-4}
-0.30	1.31	166.7	0.78	0.17	96.26	0.34	9.8×10^{-4}
-0.35	1.31	137.3	0.82	0.16	118.11	0.24	5.1×10^{-4}
-0.40	1.30	134.2	0.79	0.14	119.02	0.20	3.8×10^{-4}

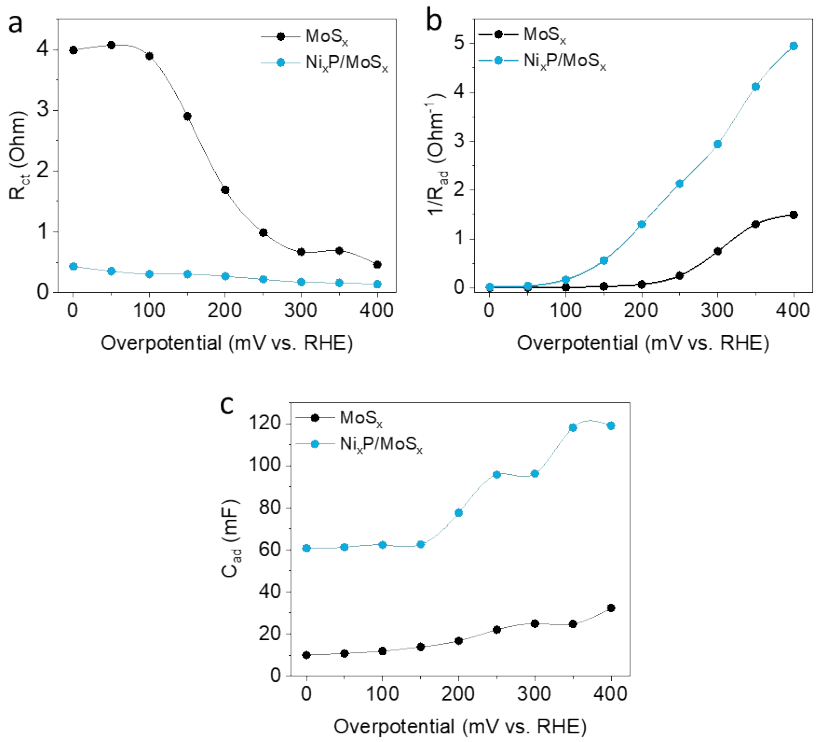

Fig. S15. Potential-dependent (a) interfacial charge-transfer resistance (R_{ct}), (b) inverse adsorption resistance ($1/R_{ad}$), and (c) adsorption pseudo-capacitance (C_{ad}) plots derived from operando EIS measurements of MoS_x and Ni_xP/MoS_x.

References

1 S. G. Quiroz, S. Cartagena and J. A. Calderón, *Electrochim. Acta*, 2025, **528**, 146332.

2 C. C. L. McCrory, S. Jung, J. C. Peters and T. F. Jaramillo, *J. Am. Chem. Soc.*, 2013, **135**, 16977–16987.

3 C. Niu, H. Song, Y. Chang, W. Hou, Y. Li, Y. Zhao, Y. Xiao and G. Han, *J. Alloys Compd.*, 2022, **900**, 163509.

4 E. A. Ponomarev, M. Neumann-Spallart, G. Hodes and C. Lévy-Clément, *Thin Solid Films*, 1996, **280**, 86–89.

5 L. Li, Y. Zhang, S. Deng and Y. Chen, *Mater. Lett.*, 2003, **57**, 3444–3448.

6 J. Xie, H. Zhang, S. Li, R. Wang, X. Sun, M. Zhou, J. Zhou, X. W. Lou and Y. Xie, *Adv. Mater.*, 2013, **25**, 5807–5813.

7 Y. Yin, J. Han, Y. Zhang, X. Zhang, P. Xu, Q. Yuan, L. Samad, X. Wang, Y. Wang, Z. Zhang, P. Zhang, X. Cao, B. Song and S. Jin, *J. Am. Chem. Soc.*, 2016, **138**, 7965–7972.

8 S. Duraisamy, A. Ganguly, P. K. Sharma, J. Benson, J. Davis and P. Papakonstantinou, *ACS Appl. Nano Mater.*, 2021, **4**, 2642–2656.

9 L. Li, Y. Zhang, S. Deng and Y. Chen, *Mater. Lett.*, 2003, **57**, 3444–3448.

10 R. N. Wasalathanthri, S. Jeffrey, N. Su, K. Sun and D. M. Giolando, *ChemistrySelect*, 2017, **2**, 8020–8027.
11 Y. R. Liu, W. H. Hu, X. Li, B. Dong, X. Shang, G. Q. Han, Y. M. Chai, Y. Q. Liu and C. G. Liu, *Appl. Surf. Sci.*, 2016, **383**, 276–282.
12 G. Q. Han, X. Li, J. Xue, B. Dong, X. Shang, W. H. Hu, Y. R. Liu, J. Q. Chi, K. L. Yan, Y. M. Chai and C. G. Liu, *Int. J. Hydrogen Energy*, 2017, **42**, 2952–2960.
13 Y. Dai, W. Chen, B. Guo, X. Li, J. Guan, L. Wang and M. Zhang, *J. Alloys Compd.*, 2022, **905**, 164157.
14 S. Hu, Q. Cao, H. Yao, Y. Jia and X. Guo, *ChemCatChem*, 2024, **16**, e202301420.
15 C. Gao, Z. Li, H. Wang, Y. Yang, B. Li, Z. Peng, J. Li and Z. Liu, *ChemElectroChem*, 2020, **7**, 355–361.
16 B. Zhang, K. Xu, X. Fu, S. Guan, X. Li and Z. Peng, *J. Alloys Compd.*, 2021, **856**, 158094.
17 T. Liang, Y. Tian, Z. Dai, S. Lenus and J. Xie, *J. Alloys Compd.*, 2023, **965**, 171416.
18 X. Yu, S. Xu, Z. Wang, S. Wang, J. Zhang, Q. Liu, Y. Luo, Y. Du, X. Sun and Q. Wu, *Dalton Trans.*, 2021, **50**, 15094–15102.